1   **Revision 1**

2

3   **Nazarovite, $Ni_{12}P_5$, a new terrestrial and meteoritic mineral structurally related to**

4   **nickelphosphide, Ni_3P**

5

6   Sergey N. Britvin[1,2]*, Mikhail N. Murashko[1], Maria G. Krzhizhanovskaya[1], Oleg S. Vereshchagin[1],

7   Yevgeny Vapnik[3], Vladimir V. Shilovskikh[4], Maksim S. Lozhkin[5], and Edita V. Obolonskaya[6]

8

9   [1] Institute of Earth Sciences, St. Petersburg State University, Universitetskaya Nab. 7/9, 199034 St.

10   Petersburg, Russia

11   [2] Kola Science Center, Russian Academy of Sciences, Fersman Str. 14, 184200 Apatity, Russia

12   [3] Department of Geological and Environmental Sciences, Ben-Gurion University of the Negev,

13   P.O.B. 653, Beer-Sheva 84105, Israel

14   [4] Centre for Geo-Environmental Research and Modeling, St. Petersburg State University,

15   Ulyanovskaya ul. 1, 198504 St. Petersburg, Russia

16   [5] Nanophotonics Resource Centre, St. Petersburg State University, Ulyanovskaya ul. 1, 198504 St.

17   Petersburg, Russia

18   [6] The Mining Museum, Saint Petersburg Mining University, 2, 21st Line, 199106 St. Petersburg,

19   Russia

20

21

22 **Abstract**

23 Nazarovite, $Ni_{12}P_5$, is a new natural phosphide discovered on Earth and in meteorites. Terrestrial

24 nazarovite originates from phosphide assemblages confined to pyrometamorphic suite of the

25 Hatrurim Formation (the Mottled Zone), the Dead Sea basin, Negev desert, Israel. Meteoritic

26 nazarovite was identified among Ni-rich phosphide precipitates extracted from the Marjalahti

27 meteorite (main group pallasite). Terrestrial mineral occurs as micrometer-sized lamella intergrown

28 with transjordanite (Ni_2P). Meteoritic nazarovite forms chisel-like crystals up to 8 μm long. The

29 mineral is tetragonal, space group $I4/m$. The unit-cell parameters of terrestrial and meteoritic

30 material, respectively: a 8.640(1) and 8.6543(3), c 5.071(3) and 5.0665(2) Å, V 378.5(2) and

31 379.47(3) Å^3, $Z = 2$. Crystal structure of terrestrial nazarovite was solved and refined on the basis of

32 X-ray single-crystal data ($R_1 = 0.0516$), whereas the structure of meteoritic mineral was refined by

33 the Rietveld method using an X-ray powder diffraction profile ($R_B = 0.22$ %). The mineral is

34 structurally similar to phosphides of schreibersite–nickelphosphide join, $Fe_3P–Ni_3P$. Chemical

35 composition of nazarovite (terrestrial/meteoritic, electron microprobe, wt.%): Ni 81.87/78.59, Fe

36 <0.2/4.10; Co <0.2/0.07, P 18.16/17.91, Total 100.03/100.67, leading to the empirical formula

37 $Ni_{11.97}P_{5.03}$ and $(Ni_{11.43}Fe_{0.63}Co_{0.01})_{12.07}P_{4.94}$, based on 17 atoms per formula unit. Nazarovite

38 formation in nature, both on Earth and in meteorites, is related to the processes of Fe/Ni

39 fractionation in solid state, at temperatures below 1100 °C.

40

41

42 **Keywords**: $Ni_{12}P_5$, nickelphosphide, Fe–Ni–P system, crystal structure, pyrometamorphism,

43 meteorite, planetary interiors, nanoprecipitates

44

Introduction

45

46   Natural phosphides belonging to the ternary system Fe–Ni–P serve as a reservoir of reduced

47   (i.e., non-phosphate) phosphorus in the Solar System (Goldstein et al. 2009; Britvin et al. 2015;

48   Litasov and Shatskiy, 2016). In material science, the crystal chemistry of Fe–Ni phosphides is the

49   foundation for the development of advanced photocatalysts and electrocatalysts (Sun et al. 2016;

50   Sun et al. 2019). In spite of a seemingly compositional simplicity, Fe–Ni–P is a quite complex

51   multiphase field which can be divided into Fe–P and Ni–P subsystems (Table 1). Iron ($Z = 26$) and

52   nickel ($Z = 28$) are near-neighbour transition metals, but their phosphides exhibit substantially

53   different chemistry and crystal chemistry (Table 1). The crystal-chemical misfits result in

54   unexpectedly restricted Fe/Ni substitutions. In fact, the joins Fe_3P–Ni_3P (schreibersite–

55   nickelphosphide) and Fe_2P–Ni_2P (barringerite–transjordanite) are the only examples of continuous

56   Fe–Ni solid solutions (Britvin et al. 2020a, 2021a). A limited Fe–Ni miscibility was reported in

57   murashkoite (Vereshchagin et al. 2021), zuktamrurite, allabogdanite (Britvin et al. 2019b) and

58   melliniite, whereas other phosphides do not show traceable Fe/Ni substitutions. The phenomenon of

59   limited miscibility opens a way to crystal-chemical Fe/Ni fractionation within reduced systems. We

60   herein report a new natural phosphide, an extreme example of such fractionation. The mineral $Ni_{12}P_5$

61   is named nazarovite, in honour of Michail Alexandrovich Nazarov (1949–2016), Russian

62   mineralogist and petrologist, for his contributions to the research of reduced meteoritic assemblages

63   (e.g., Anand et al., 2004; Nazarov et al. 2009). Both the mineral and its name have been approved by

64   the Commission on New Minerals, Nomenclature and Classification, International Mineralogical

65   Association (IMA 2019-013). The holotype specimen of nazarovite from the Hatrurim basin is

66   deposited in the collection of the Fersman Mineralogical Museum, Russian Academy of Sciences,

67   Moscow, Russia, with the registration number 5381/1.

68

69

70   **Samples and methods**

71   **Terrestrial nazarovite (the holotype material)**

72   The mineral was discovered among phosphide assemblages confined to the rocks of the

73   Hatrurim Formation (the Mottled Zone) – a huge pyrometamorphic complex spanning the Middle

74   East in Israel, West Jordan and West Bank (Gross 1977; Vapnik et al. 2007; Novikov et al. 2013).

75   Nazarovite occurs in the specimens of altered diopside microbreccia collected along the Halamish

76   wadi, Hatrurim basin, Negev desert, Israel (e.g., Britvin et al. 2021b). It was studied in conventional

77   polished thick rock sections.

78

79   **Nazarovite from the Marjalahti pallasite**

80   An acid-resistant precipitate was obtained from a piece of the metal taken from the same

81   meteorite slice where keplerite, $Ca_9(Ca_{0.5}\square_{0.5})Mg(PO_4)_7$, was recently described (specimen MM74/2,

82   the Mining Museum) (Britvin et al. 2021d). A ~0.5 cm (Fe,Ni) metal chunk, free of olivine and

83   chromite rims, was preliminarily treated in hot 10 % HCl for 1 minute, in order to clean it up from

84   surface contaminants. The etched piece was rinsed off by distilled water and then immersed into 10

85   mL of hot 10 % HCl, in 50 mL glass baker on a hot plate. After complete dissolution of acid-soluble

86   α-(Fe,Ni) (kamacite), the liquid with the insoluble residue was mixed with ~30 mL of methanol and

87   allowed to stay for 20 min, followed by gentle removal of the solution with a 20 mL syringe until ~1

88   cm level of residual liquid remained. This wash-up procedure was repeated 5 times, and after that

89   the remaining liquid with precipitate was transferred onto a watch glass and air-dried. The residue

90   was comprised by a few mm-sized grains of schreibersite, $(Fe,Ni)_3P$, and taenite, γ-(Fe,Ni). In

91   addition, a tiny film of white color with straw-yellowish tint and metallic luster was observed at the

92   bottom of the glass. It was found that the film is a microgranular phosphide precipitate which was

93   harvested into a drop of epoxy resin. The soft acid treatment of meteoritic iron applied herein

94   follows the method used in the metallurgy for the liberation of phosphide precipitates from the Ni-

95 based alloys (e.g., Lee et al., 1996). It is noteworthy that this procedure does not lead to the

96 appearance of new phosphide phases, therefore nazarovite is not a newly formed phosphide. The

97 obtained phosphide precipitate sample was first subjected to X-ray powder diffraction study and

98 later on, after embedding and polishing procedures, to electron microprobe analysis.

99

100 **Electron microprobe analysis (EMPA) and electron backscatter diffraction (EBSD)**

101 EMPA data were obtained using an Oxford Instruments AzTec Energy X-Max 20 EDX

102 spectrometer (20 kV, 1 nA) attached to a Hitachi S-3400N SEM. Cobalt was determined separately

103 using an INCA WAVE 500 WDX spectrometer (20 kV, 15 nA). Pure Ni, Fe and Co metals, along

104 with InP were used as standards. Electron backscatter diffraction (EBSD) mapping was carried out

105 on the section etched for 20 min with an Ar-ion beam generated by an Oxford Instruments IonFab-

106 300 instrument. Diffraction pattern acquisition was carried out with an Oxford Instruments Nordlys-

107 HKL detector operated at 30 kV and 1.5 nA on the sample coated with ~2 nm carbon film and glued

108 onto a 70 ° tilted stage. The EBSD patterns matching and mapping were performed using the

109 structural models of $Ni_{12}P_5$ (Rundqvist and Larsson 1959) and transjordanite end-member, Ni_2P

110 (Britvin et al. 2020a).

111

112 **Powder X-ray diffraction (PXRD) and Rietveld refinement**

113 Powder diffraction patterns were obtained by the use of a Rigaku RAXIS Rapid II

114 diffractometer (Table 2). The instrument has a Co$K\alpha$-radiation source (rotating anode, 40 kV, 15

115 mA), microfocus mirror monochromator and semi-cylindrical imaging plate detector ($r = 127.4$

116 mm). The images were acquired in Debye-Scherrer geometry (Gandolfi-type rotation). A plate-to-

117 profile data conversion was performed with the osc2xrd program (Britvin et al. 2017). Further

118 processing of the pattern of the terrestrial nazarovite-transjordanite grain was carried out with Stoe

119 WinXPOW software (Stoe and Cie GmbH). Rietveld refinement of the powder profile obtained

120   from the meteoritic precipitate (Supplementary Fig. S1) was carried out with Bruker TOPAS v.5.0

121   software (Bruker AXS). The basic refinement details and refined fractional coordinates are given in

122   Supplemental Tables S1 and S2.

123

Single-crystal X-ray diffraction (SCXRD)

125   SCXRD data were obtained only for terrestrial nazarovite; they were collected by means of a

126   Bruker Kappa APEX DUO diffractometer (1024K CCD detector). The crystal used for the study is

127   depicted in Figure 1. Because of the small size of nazarovite lamella, we did not extract them from

128   the surrounding transjordanite matrix. Instead, the whole two-phase grain was subjected to data

129   collection. A single-crystal nazarovite domain (UB-matrix) could be separated from several

130   transjordanite UB-matrices using CrysAlisPro software (Rigaku Oxford Diffraction), followed by a

131   standard set of data reduction procedures. The crystal structure of terrestrial nazarovite was solved

132   and refined to $R_1 = 0.0516$ using the *SHELX*-2018 set of programs (Sheldrick 2015) incorporated

133   into Olex2 GUI (Dolomanov et al. 2006). A summary of data collection and structure refinement

134   details is given is Supplementary Table 3. The detailed information can be retrieved from the CIF

135   file attached to Supplementary Data.

136

137   **Results**

138   **Occurrence and general appearance**

139   Microcrystalline diopside constitutes up to 80 % of microbreccia containing phosphide

140   minerals, whereas the interstices are filled with secondary thaumasite, ettringite and unidentified

141   Mg-Fe hydrous silicates. The accessory minerals are comprised by hematite, magnetite, and diverse

142   Fe-Ni phosphides (Britvin et al. 2021c). Nazarovite occurs as single-crystal lamella up to 10 μm

143   long penetrating the grain of transjordanite, Ni_2P (Fig. 1). EBSD mapping reveals that all nazarovite

144   lamella exposed onto the section surface have the same crystallographic orientation, whereas

6

145   surrounding transjordanite forms a patchy polycrystalline aggregate (Fig. 1d-f). Nazarovite-

146   transjordanite intergrowths have white colour in reflected light; both minerals are indistinguishable

147   from each other under the polarizing microscope. Due to very small size of nazarovite lamella, the

148   microhardness and reflectance values of the mineral could not be measured.

149   Nazarovite of meteoritic origin was identified in microgranular precipitates obtained by

150   dissolution of α-(Fe,Ni) metal (kamacite) of the Marjalahti meteorite (main-group pallasite). The

151   dominant phase of precipitates is acicular to thin-prismatic nickelphosphide, $(Ni,Fe)_3P$, which

152   accounts for 85-90 wt.% of acid-resistant residue (Supplementary Fig. S1). Nazarovite occurs as

153   chisel-like crystals up to 8 μm wide and 3 μm thick disseminated among nickelphosphide (Fig. 2).

154

155   **Crystal structure**

156   The unit-cell parameters of terrestrial and meteoritic nazarovite are almost identical, in

157   agreement with the composition approaching pure $Ni_{12}P_5$ (Table 3). The crystal structure of the

158   mineral contains 2 independent Ni positions and 2 P sites (Table 4). The Ni(1) atom is coordinated

159   by 12 atoms – 5Ni(1), 3Ni(2), 3P(1), and 1P(2). Ni(2) has 15-fold coordination – by 6Ni(1), 5Ni(2),

160   and 4P(1). Phosphorus atoms, P(1) and P(2), are surrounded solely by Ni and have coordination

161   numbers 10 and 8, respectively. Due to a relative simplicity of the P-centered polyhedra, the

162   nazarovite structure can be better illustrated in a phosphorus-centered approach (Fig. 3), in contrast

163   to the early descriptions of synthetic $Ni_{12}P_5$ based on the metal-centered polyhedra (Rundqvist and

164   Larsson 1959; Larson 1965). The nazarovite framework (Fig. 3a,b) is topologically similar to that of

165   the minerals belonging to schreibersite–nickelphosphide join, $Fe_3P–Ni_3P$ (Britvin et al. 2021a). Both

166   nazarovite and nickelphosphide are tetragonal, have very similar lattice metrics (Table 3), and the

167   relationship between their unit-cell contents can be expressed as $2×Ni_{12}P_5$ ($Ni_{24}P_{10}$) ↔ $8×Ni_3P$

168   ($Ni_{24}P_8$). It can be seen that the nazarovite cell contains by 2 P atoms more than that of

169   nickelphosphide. These additional P(2) atoms are inserted approximately into the positions which

7

170   are vacant in the structure of nickelphosphide (Fig. 3). The P(2) coordination polyhedron of

171   nazarovite represents an almost perfect cube [PNi$_8$]. The introduction of [PNi$_8$] cubes into the lattice

172   results in its symmetrization, manifested by the conversion from the space group $I\bar{4}$ (Ni$_3$P) to $I4/m$

173   (Ni$_{12}$P$_5$). The additional effect of phosphorus incorporation is a relative stretching of the lattice

174   along the c-axis that is manifested in the increase of the c/a ratio (Table 3).

175

176   **Chemical composition**

177   The appearance of an additional P(2) site in nazarovite (relative to nickelphosphide) results

178   in the abrupt decrease of the structural tolerance towards Fe substitution. As was already mentioned,

179   Ni$_3$P (nickelphosphide) forms a continuous series of solid solutions with Fe$_3$P (schreibersite) (Table

180   1). In contrast, both occurrences of nazarovite show the compositions either approaching or exactly

181   matching end-member Ni$_{12}$P$_5$ (Table 5). The marked difference in the affinity of respective

182   phosphides towards Fe is illustrated by the comparison of both minerals from the Marjalahti

183   pallasite, where nazarovite has a Ni/Fe ratio of more than 18, whereas the same ratio in

184   nickelphosphide is just 2 (Table 5). Such a difference is not an occasional one, but is supported by

185   the studies on synthetic systems: Fe$_{12}$P$_5$ does not exist in the Fe–P phase diagram, and Fe does not

186   substitute for Ni in synthetic Ni$_{12}$P$_5$ (Drábek 2006). Therefore, the extreme Ni enrichment of natural

187   nazarovite can be considered as its intrinsic property rather than a geochemical curiosity.

188

189   **Discussion**

190   Nazarovite is an example of the influence of crystal-chemical factors on the elemental

191   differentiation in the Fe–Ni–P system. In both terrestrial and meteoritic environments, the mineral

192   was evidently formed in the solid state at temperatures below 1100 °C, as it can be deduced from the

193   studies of the Ni–P phase diagram (Schmetterer et al. 2009). The results of EBSD and X-ray single-

194   crystal study suggest that spatially separated nazarovite lamellae shown in Figure 1 represent the

8

195   subdomains (the remnants?) of the same single crystal. The latter implies that nazarovite may in fact

196   be a primary, earlier phase in the assemblage, whereas surrounding patchy transjordanite is a

197   subsequent one, possibly formed via solid-state substitution of nazarovite.

198   The Marjalahti is one of a few witnessed pallasite falls (see a historical summary in Britvin

199   et al. 2021d). The fragments of this meteorite, harvested immediately after the fall, were not affected

200   by terrestrial weathering; thereby nazarovite in the Marjalahti has a cosmic origin, rather than being

201   a product of surficial alteration of schreibersite $(Fe,Ni)_3P$, as it was discussed with respect to

202   barringerite, $(Fe,Ni)_2P$ (Buseck 1969; Britvin et al. 2020a). The identification of nazarovite in

203   phosphide assemblages is hampered due to its compositional similarity to nickelphosphide,

204    $(Ni,Fe)_3P$, and transjordanite, $(Ni,Fe)_2P$. However, there is evidence that this phosphide may be

205   more widespread in nature. Armstrong et al. (1987) described mm-sized fremdlinge (sulphide- and

206   metal-rich droplets) within the B-type calcium-aluminium inclusion (CAI) of the Allende meteorite,

207   a CV3 carbonaceous chondrite. Among other opaque phases, Armstrong et al. (1987) reported a Ni

208   phosphide containing 80–81 wt.% Ni and less than 0.5 wt.% Fe. The authors calculated a phosphide

209   formula of Ni_5P_2, but the assumed ideal Ni/P atomic ratio of 2.5 is quite close to that of 2.4 in

210   nazarovite (Table 1). Garvie (2019) described Ni-rich phosphide nanoprecipitates from the Odessa

211   octahedrite, containing both nickelphosphide (the major phase) and the second phosphide that can

212   be attributed to either $Ni_{12}P_5$ (i.e., nazarovite) or Ni_8P_3. Taking into account that Odessa belongs to

213   the most common IAB group of iron meteorites whereas Marjalahti is a typical main-group pallasite,

214   we propose that the similar Ni-rich phosphide precipitates can be extracted from acid-resistant

215   residues of many metal-rich meteorites.

216

217   **Implications**

218   The study of natural Ni and Fe phosphides expands our knowledge of the phase relations

219   within Fe-Ni metal-rich assemblages, which are thought to constitute planetary interiors of celestial

9

220   bodies. The presence of nazarovite determines the upper thermal limit of 1100 °C for the formation

221   of its assemblages, and opens the opportunities for determination of pressure stability limits. The

222   influence of crystal-chemical factors on the processes of elemental differentiation in reduced

223   systems is a largely obscure field of mineralogy and geochemistry. Here the most prominent is the

224   Fe-Ni system (e.g., Goldstein et al. 2009), where the formation of γ-(Fe,Ni) (taenite) succeeds in

225   further selective enrichment of this phase in Ni relative to coexisting α-(Fe,Ni) (kamacite). The

226   much less studied are Fe-Ni carbide systems, where haxonite, $(Fe,Ni)_{23}C_6$, is always and

227   considerably enriched in Ni as compared to cohenite, $(Fe,Ni)_3C$ (Krot et al. 1997; Scott and

228   Goldstein 2012), but the reason for such a behavior is unclear. Among natural phosphides, one can

229   mention the selective affinity of Co towards allabogdanite, the high-pressure modification of

230    $(Fe,Ni)_2P$ (Britvin et al. 2019b). The present paper contributes to this area of planetary science, at

231   the junction between crystal chemistry and cosmochemistry. From the methodological point of

232   view, this study illustrates how advances in the X-ray instrumentation enhance the quality of crystal-

233   chemical research, in particular in meteoritics and planetary science. The full-scale structural study

234   of μm-sized mineral grains is now achievable using standard in-house instruments – a step toward

235   complementary to the fingerprint techniques like EBSD and the Laue X-ray method.

236

244   Microanalysis, Nanophotonics, Nanotechnology and Geomodel Resource Centres of St. Petersburg

245   State University for the access to instrumental and computational resources.

246

247   **References cited**

248   Anand, M., Taylor, L.A., Nazarov, M.A., Shu, J., Mao, H.-K., and Hemley, R.J. (2004) Space

249   weathering on airless planetary bodies: Clues from the lunar mineral hapkeite. Proceedings of

250   the National Academy of Sciences of the United States of America, 101, 6847–6851.

251   Armstrong, T., Hutcheon, I.D., and Wasserburg, G.J. (1987) Zelda and company: petrogenesis of

252   sulfide-rich Fremdlinge and constraints on solar nebula processes. Geochimica et

253   Cosmochimica Acta, 51, 3155–3173.

254   Britvin, S.N., Kolomensky, V.D., Boldyreva, M.M., Bogdanova, A.N., Kretser, Yu.L., Boldyreva,

255   O.N., and Rudashevskii, N.S. (1999) Nickelphosphide, $(Ni,Fe)_3P$, the nickel analog of

256   schreibersite. Proceedings of Russian Mineralogical Society, 128, 64–72 (in Russian).

257   Britvin, S.N., Murashko, M.N., Vapnik, Ye., Polekhovsky, Yu.S., and Krivovichev, S.V. (2015)

258   Earth's phosphides in Levant and insights into the source of Archaean prebiotic phosphorus.

259   Scientific Reports, 5, 8355.

260   Britvin, S.N., Dolivo-Dobrovolsky, D.V., Krzhizhanovskaya, M.G. (2017) Software for processing

261   the X-ray powder diffraction data obtained from the curved image plate detector of Rigaku

262   RAXIS Rapid II diffractometer. Zapiski Rossiyskogo Mineralalogicheskogo Obshchestva,

263   146, 104–107 (in Russian).

264   Britvin, S.N., Murashko, M.N., Vapnik, Ye., Polekhovsky, Yu.S., Krivovichev, S.V., Vereshchagin,

265   O.S., Vlasenko, N.S., Shilovskikh, V.V., and Zaitsev, A.N. (2019a) Zuktamrurite, FeP_2, a new

266   mineral, the phosphide analogue of löllingite, $FeAs_2$. Physics and Chemistry of Minerals, 46,

267   361–369.

268   Britvin, S.N., Shilovskikh, V.V., Pagano, R., Vlasenko, N.S., Zaitsev, A.N., Krzhizhanovskaya,

269   M.G., Lozhkin, M.S., Zolotarev, A.A., and Gurzhiy, V.V. (2019b) Allabogdanite, the high-

270   pressure polymorph of $(Fe,Ni)_2P$, a stishovite-grade indicator of impact processes in the Fe–

271   Ni–P system. Scientific Reports, 9, 1047.

272   Britvin, S.N., Vapnik, Ye., Polekhovsky, Yu.S. and Krivovichev, S.V., Krzhizhanovkaya M.G.,

273   Gorelova L.A., Vereshchagin, O.S., Shilovskikh, V.V., and Zaitsev, A.N. (2019c)

274   Murashkoite, FeP, a new terrestrial phosphide from pyrometamorphic rocks of the Hatrurim

275   Formation, Southern Levant. Mineralogy and Petrology, 113, 237–248.

276   Britvin, S.N., Murashko, M.N., Vapnik, Ye., Polekhovsky, Yu.S., Krivovichev, S.V.,

277   Krzhizhanovskaya, M.G., Vereshchagin, O.S., Shilovskikh, V.V., and Vlasenko, N.S. (2020a)

278   Transjordanite, Ni_2P, a new terrestrial and meteoritic phosphide, and natural solid solutions

279   barringerite–transjordanite (hexagonal Fe_2P–Ni_2P). American Mineralogist, 105, 428–436.

280   Britvin, S.N., Murashko, M.N., Vapnik, Ye., Polekhovsky, Yu.S., Krivovichev, S.V., Vereshchagin,

281   O.S., Shilovskikh, V.V., Vlasenko, N.S., and Krzhizhanovskaya, M.G. (2020b) Halamishite,

282   Ni_5P_4, a new terrestrial phosphide in the Ni–P system. Physics and Chemistry of Minerals,

283   2020, 3.

284   Britvin, S.N., Murashko, M.N., Vapnik, Ye., Polekhovsky, Yu.S., Krivovichev, S.V., Vereshchagin,

285   O.S., Shilovskikh, V.V., and Krzhizhanovskaya, M.G. (2020c) Negevite, the pyrite-type NiP_2,

286   a new terrestrial phosphide. American Mineralogist, 105, 422–427.

287   Britvin, S.N., Krzhizhanovskaya, M.G., Zolotarev, A.A., Gorelova, L.A., Obolonskaya, E.V.,

288   Vlasenko, N.S., Shilovskikh, V.V., and Murashko, M.N. (2021a) Crystal chemistry of

289   schreibersite, $(Fe,Ni)_3P$. American Mineralogist, 106, 10.2138/am-2021-7766

290   Britvin, S.N., Murashko, M.N., Vapnik ,Ye., Vlasenko, N.S., Krzhizhanovskaya, M.G.,

291   Vereshchagin, O.S., Bocharov, V.N., and Lozhkin, M.S. (2021b) Cyclophosphates, a new

292   class of native phosphorus compounds, and some insights into prebiotic phosphorylation on

293   early Earth. Geology, 49, 382–386.

294   Britvin, S.N., Vereshchagin, O.S., Shilovskikh, V.V., Krzhizhanovskaya, M.G., Gorelova, L.A.,

295   Vlasenko, N.S., Pakhomova, A.S., Zaitsev, A.N., Zolotarev, A.A., Bykov, M., Lozhkin, M.S.,

296   and Nestola, F. (2021c) Discovery of terrestrial allabogdanite $(Fe,Ni)_2P$, and the effect of Ni

297   and Mo substitution on the barringerite-allabogdanite high-pressure transition. American

298   Mineralogist, 106, 944–952.

299   Britvin, S.N., Galuskina, I.O., Vlasenko, N.S., Vereshchagin, O.S., Bocharov, V.N.,

300   Krzhizhanovskaya, M.G., Shilovskikh, V.V., Galuskin, E.V., Vapnik, Ye., and Obolonskaya,

301   E.V (2021d) Keplerite, $Ca_9(Ca_{0.5}\square_{0.5})Mg(PO_4)_7$, a new meteoritic and terrestrial phosphate

302   isomorphous with merrillite, $Ca_9NaMg(PO_4)_7$. American Mineralogist, 106, 10.2138/am-2021-

303   7834

304   Buseck, P.R. (1969) Phosphide from meteorites: Barringerite, a new iron-nickel mineral. Science,

305   165, 169–171.

306   Dolomanov, O.V., Bourhis, L.J., Gildea, R.J., Howard, J.A., and Puschmann, H. (2009) OLEX2: a

307   complete structure solution, refinement and analysis program. Journal of Applied

308   Crystallography, 42, 339–341.

309   Dowty, E. (2006). ATOMS for Windows. Shape Software, Kingsport, Tennessee, USA.

310   Drábek, M. (2006) Phosphide solid-solutions within the metal-rich portion of the quaternary system

311   Co–Fe–Ni–P AT 800°C, and mineralogical implications. Canadian Mineralogist, 44, 399–408.

312   Garvie, L.A.J. Germanium- and gallium-rich nickel phosphide "Ni_3P" nanoprecipitates from the

313   Odessa (IAB-MG) iron meteorite. 50th Lunar and Planetary Science Conference, Abstract

314   #2639.

315   Goldstein, J.I., Scott, E.R.D., and Chabot, N.L. (2009) Iron meteorites: Crystallization, thermal

316   history, parent bodies, and origin. Chemie der Erde, 69, 293–325.

13

317   Gross, S. (1977) The mineralogy of the Hatrurim Formation, Israel. Geological Survey of Israel

318   Bulletin, 70, 1–80.

319   Ilnitskaya, O.N., Akselrud, L.G., Mikhalenko, S.I., and Kuzma, Yu.B. (1987) Crystal structure of

320   alpha-Ni_8P_3. Kristallografiya, 32, 50–54 (in Russian).

321   Jeitschko, W., and Braun, D.J. (1978) Synthesis and crystal structure of the iron polyphosphide

322   FeP_4. Acta Crystallographica, B34, 3196–3201.

323   Krot, A.N., Zolensky, M.E., Wasson, J.T., Scott, E.R.D., Keil, K., and Ohsumi, K. (1997) Carbide

324   magnetite assemblages in type 3 ordinary chondrites. Geochimica et Cosmochimica Acta, 61,

325   219–237.

326   Larsson, E. (1965) An X-ray investigation of the Ni-P system and the crystal structures of NiP and

327   NiP_2. Arkiv för Kemi, 23, 335–365.

328   Lee, H.-J., Akiyama, E., Habazaki, H., Kawashima, A., Asami, K., and Hashimoto, K. (1996) The

329   effect of phosphorus addition on the corrosion behavior of arc-melted Ni-10Ta-P alloys in 12

330   M HCl. Corrosion Science, 38, 469–485.

331   Litasov, K., and Shatskiy, A. (2016) Composition of the Earth's core: a review. Russian Geology

332   and Geophysics, 57, 22–46.

333   Nazarov, M.A., Kurat, G., Brandstaetter, F., Ntaflos, T., Chaussidon, M., and Hoppe, P. (2009)

334   Phosphorus-bearing sulfides and their associations in CM chondrites. Petrology, 17, 101–123.

335   Novikov, I., Vapnik, Ye., and Safonova, I. (2013) Mud volcano origin of the Mottled Zone,

336   Southern Levant. Geoscience Frontiers, 4, 597–619.

337   Oryshchyn, S., Babizhetskii, V.S., Chikhrii, S.I., Akselrud, L.G., Stojko, S., Bauer, D., Guerin, P.,

338   and Kuzma, Yu.B. (2004) Crystal structure of Ni_5P_2. Neorganicheskie Materialy, 40, 450–456

339   (in Russian).

340   Pratesi, G., Bindi, L., and Moggi-Cecci, V. (2006) Icosahedral coordination of phosphorus in the

341   crystal structure of melliniite, a new phosphide mineral from the Northwest Africa 1054

342   acapulcoite. American Mineralogist, 91, 451–454.

343   Rundqvist, S., and Ersson, N.O. (1969) Structure and bonding in skutterudite-type phosphides.

344   Arkiv för Kemi, 30, 103–115.

345   Rundqvist, S., and Larsson, E. (1959) The crystal structure of $Ni_{12}P_5$. Acta Chemica Scandinavica,

346   13, 551–560.

347   Schmetterer, C., Vizdal, J., and Ipser, H. (2009) A new investigation of the system Ni–P.

348   Intermetallics, 17, 826–834.

349   Scott, E.R.D., and Goldstein, J.I. (2012) Occurrence of carbides and graphite in iron meteorites and

350   origin of C-rich irons. Lunar Planetary Science, 43, #2671 (abstract).

351   Sheldrick, G.M. (2015) Crystal structure refinement with *SHELXL*. Acta Crystallographica, C71, 3–

352   8.

353   Skála, R., and Drábek, M. (2003) Nickelphosphide from the Vicenice octahedrite: Rietveld crystal

354   structure refinement of a synthetic analogue. Mineralogical Magazine, 67, 783–792.

355   Sugitani, M., Kinomura, N., Koizumi, M., and Kume, S. (1978) Preparation and properties of a new

356   iron phosphide FeP_4. Journal of Solid State Chemistry, 26, 195–201.

357   Sun, M., Liu, H., Qu, J., and Li, J. (2016) Earth-Rich Transition Metal Phosphide for Energy

358   Conversion and Storage. Advanced Energy Materials, 6, 1600087.

359   Sun, Z., Zhu, M., Lv, X., Liu, Y., Shi, C., Dai, Y., Wang, A, and Majima, T. (2019) Insight into Iron

360   Group Transition Metal Phosphides (Fe_2P, Co_2P, Ni_2P) for Improving Photocatalytic

361   Hydrogen Generation. Applied Catalysis B: Environmental, 246, 330–336.

362   Vapnik, Ye., Sharygin, V.V., Sokol, E.V., and Shagam, R. (2007) Paralavas in a combustion

363   metamorphic complex: Hatrurim Basin, Israel. The Geological Society of America, Reviews in

364   Engineering Geology, 18, 133–153.

365   Vereshchagin, O.S., Pankin, D.V., Smirnov, M.B., Vlasenko, N.S., Shilovskikh, V.V., and Britvin,

366   S.N. (2021) Raman spectroscopy: A promising tool for the characterization of transition metal

367   phosphides. Journal of Alloys and Compounds, 853, 156468.

368   **List of figure captions**

369

370   **Figure 1.** Nazarovite in the phosphide assemblage of the Hatrurim Basin. (a) Polished section in

371   reflected light. Phosphide grain within the weathered silicate paralava. (b) The same grain, BSE

372   image with enhanced contrast. A series of tiny nazarovite lamellae (light) penetrate transjordanite

373   matrix. The biggest lamella was used for the structure solution and refinement. (c) EBSD phase map

374   of the same grain (nazarovite is yellow, transjordanite is green). (d) EBSD map in inverse pole

375   figure (IPF) colouring. Note that all nazarovite lamellae (blue) are represented by single crystals,

376   whereas encasing transjordanite forms a polycrystalline aggregate (patchy areas). (e) EBSD pole

377   figure of nazarovite in the area depicted in (d), projection onto {001}. Note that all nazarovite

378   lamellae have coincident crystallographic orientation, with the c-axis approximately parallel to the

379   image plane. (f) EBSD pole figure of transjordanite in the same area – a polycrystal consisting of at

380   least 3 randomly oriented domains. Abbreviations: Nz – nazarovite, Tj – transjordanite (Ni_2P), Mgt

381   – magnetite.

382

383   **Figure 2.** Nazarovite crystal (Nz) among an aggregate of nickelphosphide crystals. Polished section

384   of acid-resistant precipitate encapsulated into epoxy resin. SEM BSE image. The Marjalahti

385   pallasite.

386

387   **Figure 3.** Crystal structures of nazarovite, $Ni_{12}P_5$, and nickelphosphide, Ni_3P, in a phosphorus-

388   centered representation. (a) Nazarovite, a slice on (001). Framework of edge-sharing P(1)-centered

389   polyhedra [PNi_{10}] (yellow) and perfect P(2)-centered cubes [PNi_8] (green). (b) A cut of the

390   nazarovite framework illustrating the alternation of [PNi_8] and empty [$\square Ni_8$] cubes interleaved along

391   the c-axis. (c) Nickelphosphide, a slice on (001) in the same orientation as of nazarovite. A

17

392   framework of edge-sharing polyhedra [$P(Ni_7P_2)$], with the narrow open channels propagating along

393   the c-axis. Drawn in ATOMS v.6 (Dowty 2006).

394

18

395 **Tables**

396 Table 1. Juxtaposition of natural and synthetic phosphides in the system Fe–Ni–P [a].

M:P atomic ratio	Fe–P join		Ni–P join		Struct. type	Ref. [b]
	Mineral	Ideal formula	Ideal formula	Mineral		
4			Ni_4P	Melliniite	Al_4Au	[1]
3	Schreibersite	Fe_3P	Ni_3P	Nickelphosphide	Ni_3P	[2]
2.67			Ni_8P_3		Ni_8P_3	[3]
2.5			Ni_5P_2		Ni_5As_2	[4]
2.4			$Ni_{12}P_5$	Nazarovite	$Ni_{12}P_5$	[5]
2	Barringerite	Fe_2P	Ni_2P	Transjordanite	Fe_2P	[6]
2	Allabogdanite	Fe_2P	Ni_2P	Orishchinite	Co_2Si	[7]
1.25			Ni_5P_4	Halamishite	Ni_5P_4	[8]
1	Murashkoite	FeP			MnP	[9]
1			NiP		NiP	[10]
0.5	Zuktamrurite	FeP_2			Marcasite	[11]
0.5			NiP_2	Negevite	Pyrite	[12]
0.33			NiP_3		Skutterudite	[13]
0.25		FeP_4			FeP_4	[14]
0.25		FeP_4			CrP_4	[15]

397

398 [a] The phases which can exist under ambient conditions (either in stable or in quenched state).

399 [b]References: [1] Pratesi et al. 2006; [2] Britvin et al. 1999, 2021a; [3] Ilnitskaya et al. 1987; [4]
400 Oryshchyn et al. 2004; [5] This work; [6] Britvin et al. 2020a; [7] Britvin et al. 2021c; [8] Britvin et
401 al. 2020b; [9] Britvin et al. 2019c; [10] Larsson 1965; [11] Britvin et al. 2019a; [12] Britvin et al.
402 2020c; [13] Rundqvist and Ersson 1969; [14] Jeitschko and Braun 1978; [15] Sugitani et al. 1978.

403

404

405

406   Table 2. Powder X-ray diffraction data for nazarovite (d in Å)

	Hatrurim basin			Marjalahti pallasite				
I_{obs}	d_{obs}	I_{calc}	d_{calc}	I_{obs}	d_{obs}	I_{calc}	d_{calc}	hkl
5	4.374	3	4.374	3	4.370	2	4.372	101
		3	4.320					200
		2	3.073	3	3.080	4	3.076	211
		2	3.054	5	3.062	4	3.060	220
		11	2.732	15	2.736	13	2.737	310
5	2.503	9	2.504	8	2.508	6	2.507	301
54	2.341	39	2.342	43	2.339	40	2.341	112
		16	2.187	[b]		18	2.186	202
		17	2.167	[b]		14	2.169	321
13	2.160	23	2.160	[b]		21	2.164	400
15 [a]	2.040	19	2.036	27	2.038	22	2.040	330
		7	1.937			4	1.939	411
40 [a]	1.931	59	1.932	69	1.934	62	1.935	420
100	1.860	100	1.859	100	1.858	100	1.859	312
		7	1.694	10	1.696	8	1.697	510
		3	1.644	5	1.643	3	1.645	402
				5	1.637	6	1.638	501
		8	1.636					431
		3	1.588					332
		5	1.537			8	1.538	422
		2	1.409	5	1.410	4	1.410	512
		3	1.381			3	1.381	323
		5	1.366	6	1.368	5	1.368	620
		9	1.279	[b]		11	1.281	532
		9	1.268	[b]		10	1.267	004
		6	1.222	[b]		9	1.224	710
		3	1.208			2	1.209	433
		13	1.203	14	1.204	18	1.204	622

407
408   [a] The line partially overlaps with the reflection from transjordanite. [b] Line completely
409   overlaps with the reflection from nickelphosphide, (Ni,Fe)$_3$P.
410

411

412   Table 3. Crystal parameters of nazarovite and synthetic end-member nickelphosphide.
413

Mineral	Nazarovite			Nickelphosphide
Locality	Hatrurim	Hatrurim	Marjalahti	Synthetic
Method	SCXRD	PXRD	Rietveld	Rietveld
Formula	$Ni_{12}P_5$	$Ni_{12}P_5$	$(Ni_{11.43}Fe_{0.67})_{12}P_5$	Ni_3P
Space group	$I4/m$	$I4/m$	$I4/m$	$I\overline{4}$
a (Å)	8.640(1)	8.639(5)	8.6543(3)	8.9546(1)
c (Å)	5.071(3)	5.072(3)	5.0665(2)	4.3871(1)
$c/a \times 10$	5.869	5.871	5.853	4.899
V (Å^3)	378.5(2)	378.6(6)	379.47(3)	351.78(2)
Z	2	2	2	8
D_x (g cm^{-1})	7.54	7.54	7.55	7.82
Reference	This work	This work	This work	Skála and Drábek 2003

414

415

416

417 Table 4. Selected interatomic bond distances (Å) for nazarovite.
418

Bond	Distance	
	Hatrurim	Marjalahti
Ni1–Ni1	2.522(3)	2.53(2)
Ni1–Ni1	2.549(3)	2.54(2)
Ni1–Ni1	2.587(3)	2.605(10)
Ni1–Ni1	2.639(2) ×2	2.647(7) ×2
Ni1–Ni2	2.540(2)	2.531(10)
Ni1–Ni2	2.574(2)	2.556(10)
Ni1–Ni2	2.705(2)	2.716(10)
Ni1–P1	2.222(3)	2.340(14)
Ni1–P1	2.424(3)	2.350(15)
Ni1–P1	2.455(3)	2.556(15)
Ni1–P2	2.252(1)	2.262(7)
Ni2–Ni2	2.544(4)	2.574(16)
Ni2–P1	2.240(4)	2.083(17)
Ni2–P1	2.242(4)	2.206(19)
Ni2–P1	2.600(2) ×2	2.571(3) ×2

419
420
421

422

423

424 Table 5. Chemical composition (wt. %) of nazarovite and associated phosphides.
425

	Hatrurim basin		Marjalahti pallasite	
	Nazarovite $n = 7$ (range)	Transjordanite $n = 6$ (range)	Nazarovite $n = 4$ (range)	Nickelphosphide $n = 5$ (range)
Ni	81.87 (81.39–82.29)	79.04 (78.26–79.73)	78.59 (78.01–79.42)	59.35 (52.90–63.92)
Fe	< 0.2	< 0.2	4.10 (3.46–5.13)	25.81 (21.22–31.37)
Co	< 0.2	< 0.2	0.07 (0.00–0.29)	0.23 (0.20–0.27)
P	18.16 (18.01–18.35)	21.01 (20.85–21.12)	17.91 (17.52–18.23)	15.01 (14.89–15.21)
Total	100.03	100.05	100.67	100.40
Formula amounts				
	$\Sigma = 17$ *apfu*	$\Sigma = 3$ *apfu*	$\Sigma = 17$ *apfu*	$\Sigma = 4$ *apfu*
Ni	11.97	1.99	11.43	2.06
Fe			0.63	0.94
Co			0.01	0.01
Σ	11.97	1.99	12.07	3.01
P	5.03	1.01	4.94	0.99

426
427
428

429

430
431
432

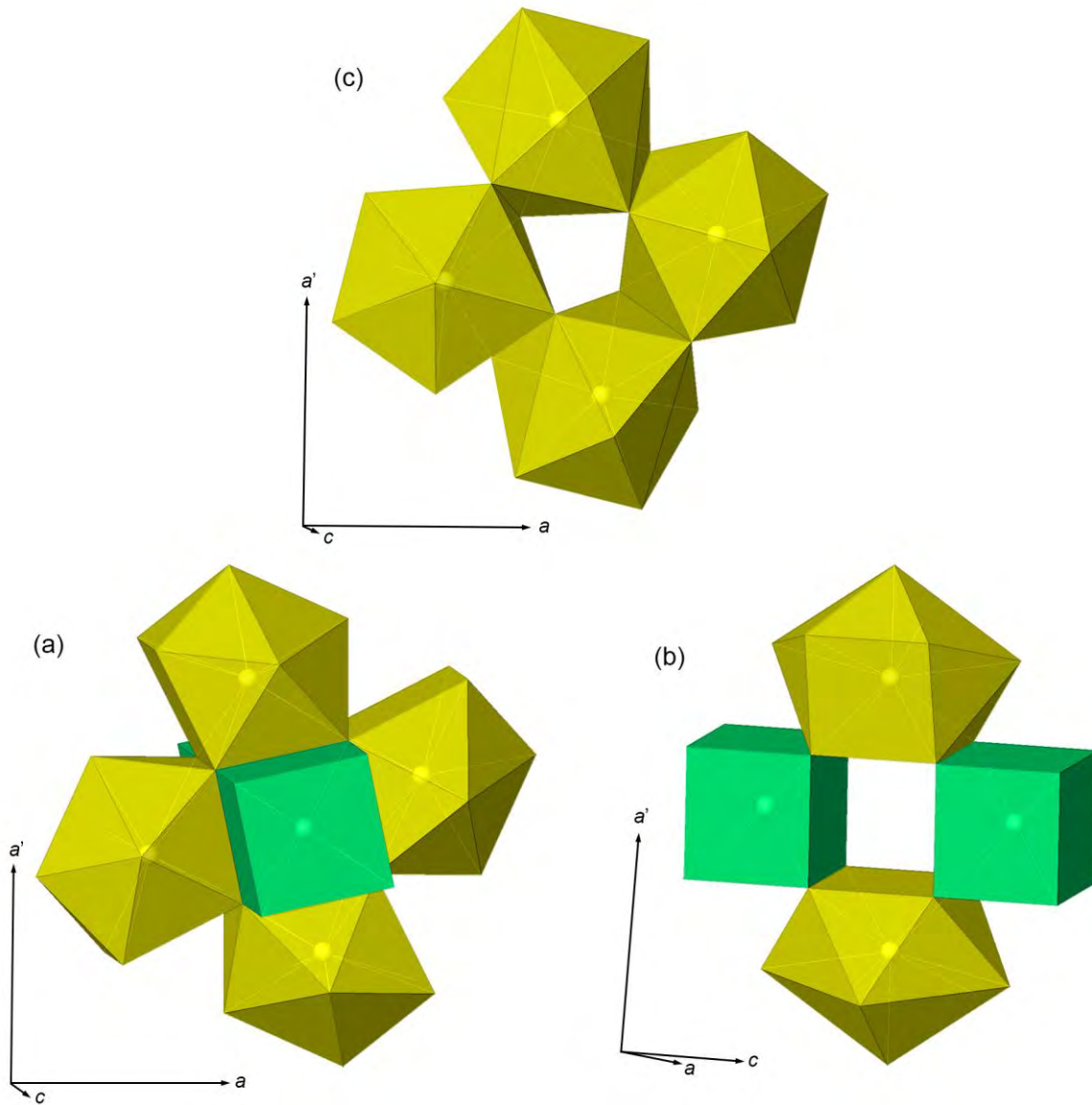433

434

435 **Figures**

436

437

438 **Figure 1**

439

24

440

441

Figure 2

442

443

444
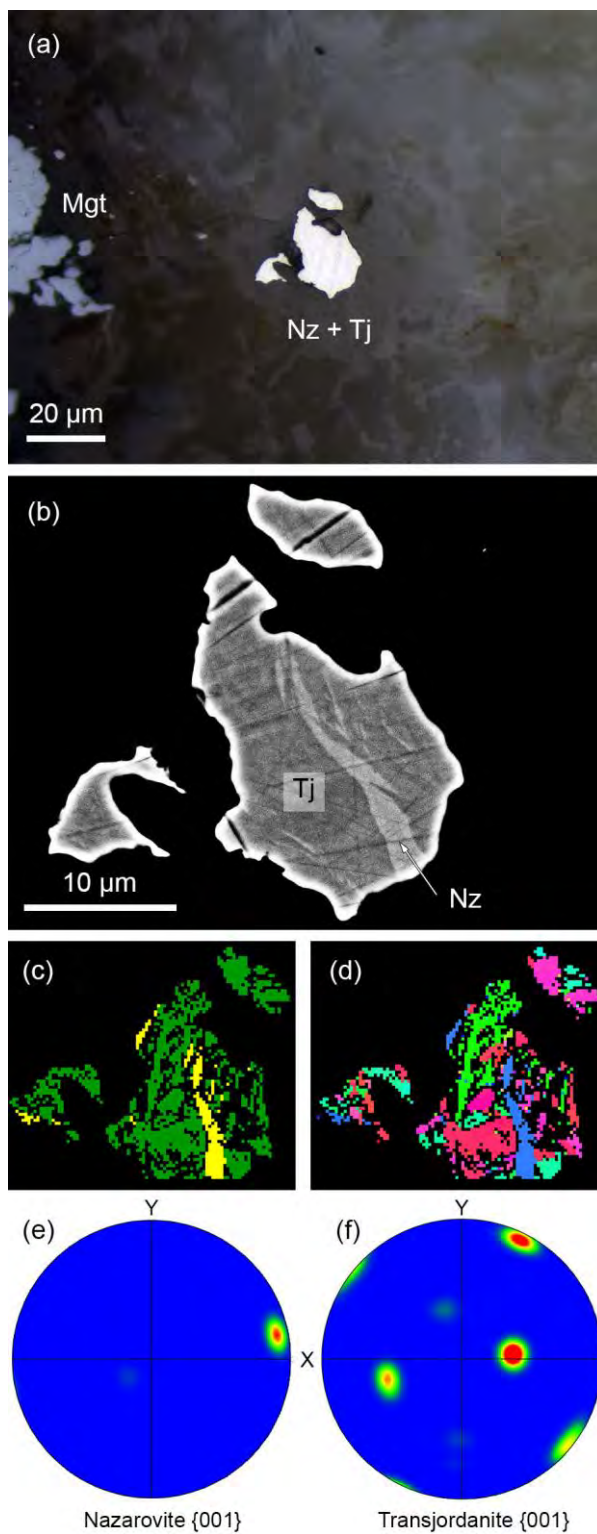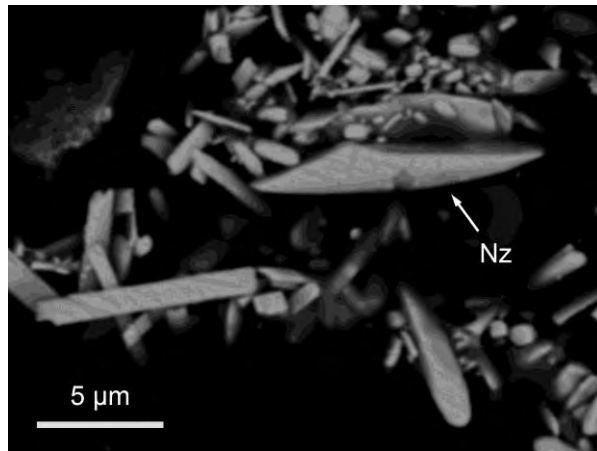
445
446

447
448

449

Figure 3